

Guided spin wave in monolayer CrSBr: Localization and spin-orbit coupling from dipolar field

D. Wang* and J. K. Vejpravová†

Department of Condensed Matter Physics, Charles University,

Ke Karlovu 5, Prague 2, 12116, Czech Republic

(Dated: January 21, 2026)

Abstract

Spin-wave spectrum of monolayer CrSBr waveguides was studied by numerically diagonalizing the Bogoliubov-de Gennes Hamiltonian derived from linearising the Landau-Lifshitz-Gilbert equation. In contrast to its short-range counterparts, the long-range dipolar field acts statically as a confining potential for spin wave, while the dynamic part couples the spin and orbit degrees of freedom, thus giving rise to spin-orbit coupling for spin wave. Due to the inversion symmetry of the Hamiltonian and the spinor structure of the wave function, spin-wave eigenstates form doublets with definite parity. Micromagnetic simulation tallies well with numerical calculation. Our study on spin-wave eigenstates in CrSBr waveguides sheds light on the nature of exchange-dipole spin wave in ferromagnetic slabs. We confirm particularly that the robustness of the Damon-Eshbach mode is not derived from topology, but rather from the static dipolar field. Moreover, a thorough knowledge on spin wave in monolayer CrSBr itself represents a step forward to understanding the more complicated antiferromagnetic resonance in bulk CrSBr.

I. INTRODUCTION

Due to their reduced dimensionality, two-dimensional (2D) materials can be affected more easily by external means such as gating electric field¹ and exhibit more quantum phenomena, one prominent example of which is the room-temperature quantum Hall effect². In spintronics, this kind of versatility is long sought-for. Hence, the experimental discovery of a 2D magnet, CrI₃³, led to intensive follow-up research in it and other 2D magnets. The catch of CrI₃ is its low Curie temperature, only about 45 K in the monolayer limit. With a relatively high Néel temperature of 132 K and air stability, CrSBr is a more promising van der Waals antiferromagnet for device integration^{4,5}.

Spin wave, or magnon after quantization, is magnetic elementary excitation that plays an important role in determining the magnetic behaviour of magnets. A well-known example is the Bloch $T^{3/2}$ law for the temperature dependence of magnetization at low temperature, caused by excitation of magnons. Spin wave is also pivotal in determining the low-frequency dynamics of magnetic topological textures. In particular, it was found that inertial skyrmion behaviour can be induced by magnons through contact interaction with a skyrmion⁶. Moreover, it can be envisioned that dynamic interaction between skyrmions could be mediated by magnons acting as intermediate bosons, in analogy with electromagnetic interaction between electrons mediated by photons.

Electromagnetic field, mainly the magnetic part, is actually an important constituent of the total effective field acting on magnetization. This kind of magnetostatic, or dipolar, field is long-range and non-local in nature, in stark contrast to other constituents of the effective field, such as the anisotropy field and the Zeeman field, which are completely short-range and local. The exchange field can be approximated as a nearest-neighbour interaction, thus making it short-range, albeit non-local. The long-range nature of the dipolar field makes it difficult to be taken into account analytically. In the *bona fide* 2D limit, a demagnetization factor -1 in the direction perpendicular to the 2D plane is enough to describe the dipolar field, contributing effectively as an easy-plane anisotropy. However, if the considered geometry is finite in any of the three dimensions, the dipolar field concentrates mostly around the boundary, due to magnetic charge accumulation therein. The localized dipolar field acts as a confining potential for spin wave and can cause spin-wave localization and effective spin-orbit coupling of magnons, similar to corresponding phenomena of electrons.

Terahertz spin wave in CrSBr was first measured by neutron scattering to extract the various exchange coupling constants⁷. Due to the small interlayer antiferromagnetic (AFM) exchange coupling, AFM resonance in the gigahertz range can also be measured⁸. Recently, the effect of the dipolar field on the AFM resonance spectrum was considered¹⁰, but there is still a lack of a systematic treatment of the dipolar-field effect on spin wave in CrSBr. In view of its potential application as magnonic devices, we will hence consider here the exchange-dipole spin wave in monolayer CrSBr, highlighting the dipolar confinement effect on spin wave in monolayer and even multilayer⁹ devices with finite lateral extension. As bulk CrSBr can be viewed as monolayers coupled together through the AFM interlayer exchange interaction, our result on spin wave in monolayer CrSBr can shed light on the interpretation of the debated AFM resonance spectrum of bulk CrSBr¹⁰.

The organization of the article is as follows. After this Introduction, in Secs. II and III, we will give the magnetic parameters and the magnetostatic Green functions that will be used in our calculation and simulation. Sec. IV will then present briefly the theoretical formulation of spin wave. Spin-wave spectra for field applied along principal crystallographic axes will be given in Secs. V, VI, and VII for an infinite film, a waveguide, and a slab of monolayer CrSBr, respectively. Our conclusion on the current investigation will be presented in Sec. IX, which is preceded by a discussion about the physical origin of the Damon-Eshbach, or edge, mode in Sec. VIII.

II. MAGNETIC PARAMETERS

The space group of CrSBr is *Pmmn*, with orthorhombic lattice constants¹¹ $a = 3.54$ Å, $b = 4.73$ Å, and $c = 7.96$ Å. The magnetic moment of CrSBr is mainly derived from Cr³⁺ ions. Using the theoretically calculated value¹¹ $3 \mu_B$ /f.u., the saturation magnetization can be easily calculated as $M_s = 4.2 \times 10^5$ A/m, which is close to the experimentally measured bulk value¹². The anisotropy constants along the b and c axes are $K_b = 5.3 \times 10^4$ J/m³ and $K_c = 2.6 \times 10^4$ J/m³, respectively, considering only the spin-orbit contribution to the anisotropy¹¹. Our K_b is slightly larger than the value 4.4×10^4 J/m³ obtained from fitting the microwave absorption spectrum¹³. Taking into account of the demagnetization energy changes the c axis into a hard axis, $K_c = -8.3 \times 10^4$ J/m³, which is smaller than the value -9.7×10^4 J/m³ determined experimentally¹³. Converting to anisotropy fields,

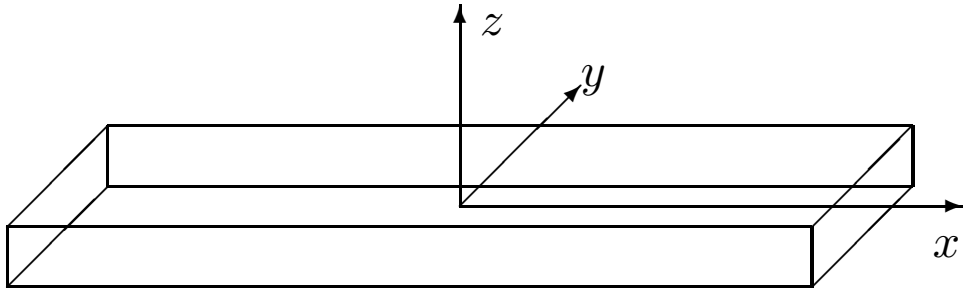


FIG. 1. Coordinate system used for spin wave in a monolayer of CrSBr. The rectangular slab is bounded by coordinate planes $x = \pm l$, $y = \pm w$, and $z = \pm t$. In the limit $l \rightarrow \infty$, the slab becomes an ideal, infinitely long, waveguide. An extended film has both $l \rightarrow \infty$ and $w \rightarrow \infty$.

$\mu_0 H_b = 0.25$ T and $\mu_0 H_c = -0.40$ T, which are significantly smaller than $\mu_0 H_b = 0.38$ T and $\mu_0 H_c = -0.92$ T obtained from AFM resonance measurements⁸. The exchange interaction between in-plane (*ab*) Cr^{3+} ions is mediated through S^{2-} or Br^- ions or both. Between two monolayers stacked along the *c* direction, the exchange interaction is mediated by two Br^- ions through the exchange path Cr-Br-Br-Cr, making the interlayer exchange coupling much smaller⁷. Using the fitted nearest-neighbour Heisenberg exchange energy $J = 1.67$ meV and $J = 1.90$ meV along *a* and *b* directions respectively, the corresponding micromagnetic exchange constants can be calculated to be $A = 1.26$ pJ/m and $A = 1.95$ pJ/m, using the relation¹⁴ $A = JS^2/d$ with *d* equal to *a* or *b* and $S = 3/2$. As the actual crystal symmetry is rhombic instead of cubic, the exchange interactions along *a* and *b* directions are different. This anisotropic character of the exchange interaction can give rise to anisotropic micromagnetic exchange interactions that will make Hopfions stable¹⁵. As the focus of the current study is on low-frequency spin wave, the complications and opportunities accompanying the anisotropic character of CrSBr will not be considered, and we approximate the anisotropic CrSBr as an isotropic Heisenberg magnet. The isotropic exchange constant is taken to be the algebraic average $A = 1.6$ pJ/m.

III. MAGNETOSTATIC GREEN FUNCTION

The dipolar field \mathbf{d} normalized to M_s depends on the magnetization configuration through the divergence-free Maxwell equation $\nabla \cdot (\mathbf{m} - \mathbf{d}) = 0$, where \mathbf{m} is the unit magnetization vector, $\mathbf{m} = \mathbf{M}/M_s$. An explicit relation between \mathbf{d} and \mathbf{m} can be obtained using the

magnetostatic Green function¹⁶, $d_i(\mathbf{r}) = (G_{ij} * m_j)(\mathbf{r})$. G_{ij} is a real symmetric tensor, where i and j can be any of the three subscripts x , y , and z . The star operator $*$ following G_{ij} designates convolution in coordinate space, $(G_{ij} * m_j)(\mathbf{r}) = \int d\mathbf{r}' G_{ij}(\mathbf{r} - \mathbf{r}') m_j(\mathbf{r}')$, where \mathbf{r} and \mathbf{r}' are general position vectors. The convolution operation demonstrates clearly the long-range characteristics of the dipolar field: \mathbf{d} at one point is determined by the whole distribution of \mathbf{m} , rather than the local value or differentiation of \mathbf{m} . Whenever there is no risk of confusion, we will omit the argument of G_{ij} . The dipolar field is given by the convolution of G_{ij} and \mathbf{m} demonstrates one important feature of the magnetostatic interaction: The dipolar field is conformal, or scale, invariant; it depends only on the relative size rather than the absolute dimension of a sample. In addition, G_{ij} satisfies the constraint $G_{ii}(\mathbf{r} - \mathbf{r}') = \delta(\mathbf{r} - \mathbf{r}')$, which reduces the independent components of G_{ij} to five: G_{xx} can be obtained from G_{yy} and G_{zz} as $G_{xx} = \delta(\mathbf{r} - \mathbf{r}') - G_{yy} - G_{zz}$. For the quasi-2D case of a thin slab of magnetic material (c.f. Fig. 1), G_{ij} 's dependence on $z - z'$ can be eliminated, through the simplifying assumption that the magnetization distribution in the thickness (z) direction is uniform. In this approximation, G_{ij} depends only on the difference of the in-plane position vectors $\boldsymbol{\rho} = \hat{x}x + \hat{y}y$ and $\boldsymbol{\rho}' = \hat{x}x' + \hat{y}y'$. \hat{x} and \hat{y} are unit vectors along the x (or crystallographic a) and y (or crystallographic b) directions.

For the study of spin wave, it is more convenient to use the Fourier transform of G_{ij} , which is defined as $G_{ij}(\mathbf{k}) = \int d\boldsymbol{\rho} G_{ij}(\boldsymbol{\rho}) \exp(-i\mathbf{k} \cdot \boldsymbol{\rho})$. The advantage of using \mathbf{k} instead of $\boldsymbol{\rho}$ can be traced back to the convolution structure $(G_{ij} * m_j)(\boldsymbol{\rho})$ which will become product in \mathbf{k} -space, $G_{ij}(\mathbf{k})m_j(\mathbf{k})$, upon Fourier transformation. Explicitly, $G_{zz}(k) = 1 - f_k$, $G_{ij}(\mathbf{k}) = k_i k_j f_k / k^2$ where the function¹⁶ $f_k = 1 - (1 - e^{-2kt})/2kt$ results from averaging over the thickness $2t$ along z , and $k = \sqrt{k_x^2 + k_y^2}$ is the modulus of \mathbf{k} . Meanwhile, the independent components of G_{ij} are reduced further from five to three: Off-diagonal components G_{zi} are averaged to zero. $G_{ij}(\mathbf{k})$ are involved in description of spin wave in infinitely extended films.

For the configuration of a waveguide with width $2w$ along \hat{y} , which will be the focus of the current study, we need the x -Fourier-transformed components $G_{ij}(k_x, y) = \int dx G_{ij}(\boldsymbol{\rho}) \exp(-ixk_x)$. The zz component can be calculated analytically¹⁶, $G_{zz}(k_x, y) = [K_0(|k_x y|) - K_0(|k_x| \sqrt{4t^2 + y^2})]/2\pi t$, where K_0 is the zeroth order modified Bessel function of the second kind. Using the uniform limit of $4\pi t G_{zz} = \ln(1 + 4t^2/y^2)$, we can calculate the

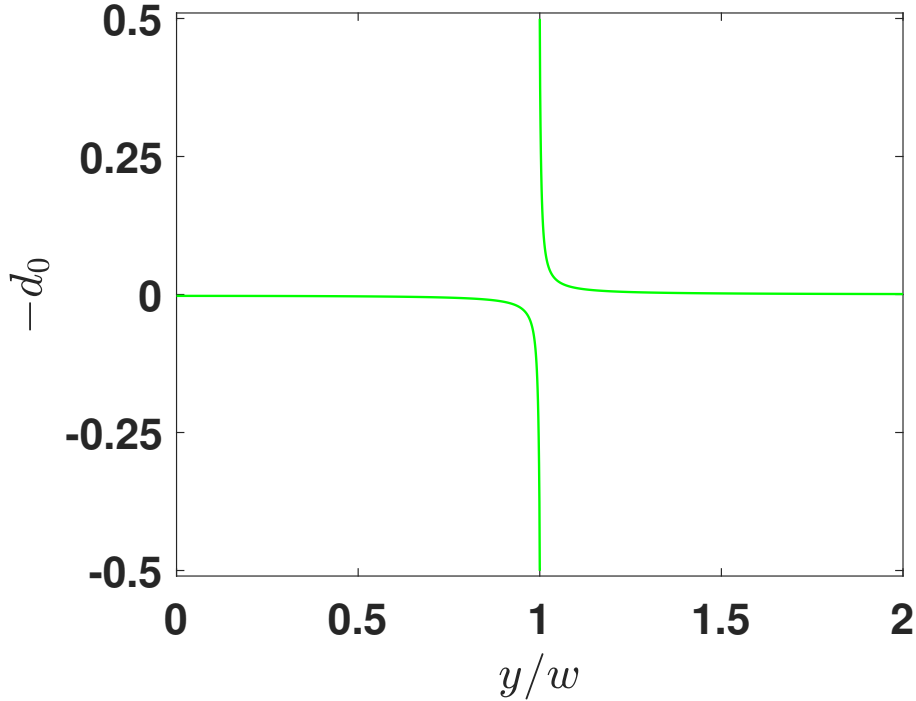


FIG. 2. Static dipolar field for a wave guide when $\mathbf{m} = \hat{y}$, Eq (1). The jump at $y = w$ is exactly 1, as required by the continuity of the \mathbf{B} field. $-d_0$ is symmetric with respect to y .

static demagnetization field when the magnetization is uniformly magnetized along \hat{y} ,

$$-\pi d_0 = \frac{w_-}{2} \ln(1 + w_-^{-2}) + \frac{w_+}{2} \ln(1 + w_+^{-2}) - \tan^{-1} w_-^{-1} - \tan^{-1} w_+^{-1} \quad (1)$$

with $w_{\pm} = (w \pm y)/2t$. As shown in Fig. 2, $-d_0$ monotonically decreases from $y = 0$ to $y = \pm w$ and can act as a symmetric confining potential for spin wave. The discontinuity of $-d_0$ at $y = \pm w$ satisfies the boundary condition imposed by the continuity of the induction (\mathbf{B}) field. Without this discontinuity, d_0 would be a continuous function over the whole y -space. Other components cannot be expressed explicitly, but their dependence on k_x is easily seen as ($i, j = x, y$) $G_{ij}(k_x, y) = \int dk_y G_{ij}(\mathbf{k}) \exp(ik_y y)/2\pi$. From those expressions, it is obvious that the diagonal components are still real, but G_{xy} is pure imaginary, $G_{xy}^*(k_x, y) = -G_{xy}(k_x, y)$, which means that the diagonal components are time-reversal even and the only non-zero off-diagonal component is odd under time-reversal.

Due to the fact that f_k depends only on k , G_{ij} are invariant under 2D inversion, $G_{ij}(k_x, y) = G_{ij}(-k_x, -y)$, i.e. the parity of G_{ij} is $P = +1$. Separate parity P_x or P_y for inversion along x or y can also be defined with the relation $P = P_x P_y$: The diagonal components have parity $P_{x,y} = +1$, $G_{ii}(k_x, y) = G_{ii}(-k_x, y) = G_{ii}(k_x, -y)$ with

$i = x, y$, or z , and the off-diagonal component has parity $P_{x,y} = -1$, $G_{xy}(k_x, y) = -G_{xy}(-k_x, y) = -G_{xy}(k_x, -y)$. This inversion symmetry is also obeyed in coordinate space¹⁶, $G_{zz} = [\rho^{-1} - \sqrt{4t^2 + \rho^2}]/4\pi t$ and $G_{ij} = -\partial^2\phi/\partial x_i\partial x_j$ ($x_{i,j} = x, y$) where the scalar function¹⁶ $\phi = [\xi - \sqrt{1 + \xi^2} + \ln(\xi^{-1} + \sqrt{1 + \xi^{-2}})]/2\pi$ with $\xi = \rho/2t$. To get those expressions in coordinate space, it is easier to start from the expression for the Green function in 3D, $G_{ij} = -\partial^2 r^{-1}/\partial x_i\partial x_j$, and then average over the z direction¹⁶. Actually, the inversion symmetry of the 2D Green function follows from the inversion symmetry of the 3D function, as the average over thickness conserves inversion symmetry in plane. $G_{ij}(\rho)$ are needed for consideration of spin wave in magnetic thin slabs.

IV. THEORETICAL FRAMEWORK

Magnetization dynamics in monolayer CrSBr is governed by the Landau-Lifshitz-Gilbert (LLG) equation¹⁷ $\dot{\mathbf{m}} = \mathbf{h} \times \mathbf{m} + \alpha \mathbf{m} \times \dot{\mathbf{m}}$ with the damping constant α . A dot over \mathbf{m} denotes the partial derivative with respect to time, $\dot{\mathbf{m}} = \partial \mathbf{m} / \partial t$. The effective magnetic field normalized to M_s is

$$\mathbf{h} = \mathbf{h}_a + \hat{y}h_b m_y + \hat{z}h_c m_z + \nabla^2 \mathbf{m} - \mathbf{d}. \quad (2)$$

\mathbf{h}_a is the externally applied field, $h_{b,c} = K_{b,c}/K_d$ are the uniaxial anisotropy fields along b and c directions, and $K_d = \mu_0 M_s^2/2$, where μ_0 is the vacuum permeability, is the dipolar energy density constant. ∇ is the gradient operator and \hat{z} is the unit vector along the z (c) direction, which is perpendicular to the xy (ab) monolayer plane. Corresponding to the dimensionless form of field, angular frequency ω (or time t) is measured in units of γM_s (or $2\pi/\gamma M_s$), where γ is the gyromagnetic constant, and length in units of the exchange length $l_{ex} = \sqrt{A/K_d}$.

The equilibrium configuration of magnetization \mathbf{m}_0 is determined by $\mathbf{m}_0 \times \mathbf{h}_0 = 0$, or equivalently the minimization of the magnetic interaction energy corresponding to the static effective field \mathbf{h}_0 , which consists of \mathbf{h}_a , the static dipolar field $-\mathbf{d}_0$ and other fields as defined in Eq. (2). In contrast to \mathbf{h}_a , even for a uniformly magnetized state, \mathbf{d}_0 is non-uniform. Once \mathbf{m}_0 is given, it is convenient to change to a coordinate system in which \mathbf{m}_0 is everywhere along the third-axis¹⁸, $\mathbf{m}_0 = \hat{e}_3$. In this local coordinate system, spin wave can be considered as excitation over \mathbf{m}_0 , $\mathbf{m} = \hat{e}_3 + \mathbf{m}_1$, together with the field decomposition $\mathbf{h} = h_0 \hat{e}_3 + \mathbf{h}_1$

to the first order of $\mathbf{m}_1 = \hat{e}_1 m_1 + \hat{e}_2 m_2$, where \hat{e}_1 and \hat{e}_2 are two unit vectors perpendicular to \hat{e}_3 , satisfying the right-handed rule $\hat{e}_1 \times \hat{e}_2 = \hat{e}_3$. The equation of motion for spin wave in the local system is then $\dot{\mathbf{m}}_1 = (\tilde{\mathbf{h}} - h_0 \mathbf{m}_1) \times \hat{e}_3$. In terms of the complex spin-wave wave function $\psi = (\psi_+, \psi_-)^T$, where $\psi_+ = m_1 + i m_2$ and ψ_- is ψ_+ 's complex conjugate, $\psi_- = \psi_+^* = m_1 - i m_2$, the dynamics of spin wave is determined by the Bogoliubov-de Gennes (BdG) equation

$$-i\sigma_z \dot{\psi} = H\psi \quad (3)$$

with the Hamiltonian

$$H = H_0 - \sigma_x H_1 - \sigma_y G_{12}^*, \quad (4)$$

where $H_0 = h_0 - \nabla^2 - (h_+ - G_+^*)/2$ and $H_1 = (h_- - G_-^*)/2$. σ_x , σ_y and σ_z are Pauli matrices, $h_\pm = h_1 \pm h_2$ with h_1 and h_2 being the anisotropy fields along \hat{e}_1 and \hat{e}_2 axes respectively, and similarly $G_\pm = G_{11} \pm G_{22}$. G_\pm and G_{12} describe the dynamic dipolar field when convoluted with ψ . Depending on the considered geometry, the convolution operation can reduce to multiplication in \mathbf{k} -space for an infinite film, 1D convolution over y for a waveguide, or 2D convolution over ρ for a slab.

σ_z on the left hand side of Eq. (3) reflects simply the symplectic structure of classical Hamilton dynamics, as the standard symplectic matrix $i\sigma_y$ is related to $-i\sigma_z$ by a unitary transformation $U = \exp(i\theta) \exp(-i\theta\sigma_x) \exp(-i\theta\sigma_z)$ with $\theta = \pi/4$, $-i\sigma_z = U^\dagger i\sigma_y U$. U corresponds to the change of variables from $\psi_\pm/\sqrt{2}$ to $m_{1,2}$. H in Eq. (4) is Hermitian. However, the solution of the BdG equation usually does not satisfy the condition $\psi_+ = \psi_-^*$, which is needed for the spin-wave interpretation. This difficulty can be resolved by the particle-hole symmetry⁶ of H , $\sigma_x H^* \sigma_x = H$, which ensures that the physical spin-wave wave function can be constructed from $\psi + \sigma_x \psi^*$. Mathematically, the particle-hole symmetry of H is a direct result of the realness of H_0 , H_1 and G_{ij} , and it is not the usual time-reversal symmetry for bosonic field¹⁹. Physically, the particle-hole symmetry of Eq. (3) corresponds to the well-known fact that spin wave is the collective motion of individual magnetic moments, which precess around their equilibrium directions; the direction of precession is determined by the gyromagnetic ratio γ , implying that changing the sign of ω cannot change the direction of precession of the underlying moments and, correspondingly, the chirality of the resultant spin wave.

Explicit expressions of G_\pm and h_\pm for field applied along three principal crystallographic

axes are listed in Table I, where \mathbf{m}_0 is assumed to be parallel to \hat{h}_a everywhere. This assumption of a uniform \mathbf{m}_0 is valid for infinite films and waveguides, as $G_{xy} \propto k_x$ is zero when $k_x = 0$. For slabs, $G_{xy} \neq 0$ and its contribution to \mathbf{d}_0 will introduce magnetization curling in the ground state, the effect of which on spin wave will be discussed briefly in Sec. VII. Table I shows clearly that G_{12} is not zero only when $\hat{h}_a = \hat{z}$. Then, according to the symmetry of G_{ij} discussed in Sec. III, the Hamiltonian H is invariant under inversion along y when \mathbf{h}_a is applied in-plane and every magnon state should have a definite parity $P_y = \pm 1$, in addition to the 2D parity $P = \pm 1$. When $\hat{h}_a = \hat{z}$, G_{xy} violates the inversion symmetry along y generally, but it vanishes at $k_x = 0$. Hence we can still label magnon states in waveguides by their y -parity P_y at $k_x = 0$. For brevity, we will still refer to the parity $P_y = \pm 1$ of a band, bearing in mind that the parity P_y refers to the whole band for \mathbf{h}_a in-plane while it is only exact for the k_x -zero state in the band when $\hat{h}_a = \hat{z}$.

\hat{h}_a	G_{\pm}	G_{12}	h_{\pm}	h_0
\hat{z}	$G_{xx} \pm G_{yy}$	G_{xy}	$\pm h_b$	$h_a + h_c - d_0$
\hat{y}	$G_{zz} \pm G_{xx}$	0	h_c	$h_a + h_b - d_0$
\hat{x}	$G_{yy} \pm G_{zz}$	0	$h_b \pm h_c$	$h_a - d_0$

TABLE I. G_{\pm} , G_{12} , h_{\pm} , and h_0 for $\hat{h}_a = \hat{x}$, \hat{y} , and \hat{z} . $-d_0$ is the static dipolar field, while G_{\pm} and G_{12} correspond to the dynamic part.

V. SPIN WAVE IN MOMENTUM SPACE

For an infinite film, spin wave should have the form $\psi \propto \exp[i(\mathbf{k} \cdot \boldsymbol{\rho} + \omega t)]$, as there is no boundary existent. The eigenequation for ω is $\omega \sigma_z \psi_k = H(\mathbf{k}) \psi_k$. The Hamiltonian in \mathbf{k} -space, $H(\mathbf{k})$, is obtained from Eq. (4) by substituting the Laplacian operator ∇^2 with $-k^2$. A rotation in spinor space with angle α_k determined by $\tan 2\alpha_k = G_{12}/H_1$ will transform $H(\mathbf{k})$ into a simpler form $H'(\mathbf{k}) = U H U^\dagger = H_0 - r_k \sigma_x$, with $r_k = (H_1^2 + G_{12}^2)^{1/2}$ and $U = \exp(i\sigma_z \alpha_k)$. Eigenvalues and eigenfunctions of $H(\mathbf{k})$, which would govern the dynamics of electrons through the corresponding Schrödinger equation with the same $H(\mathbf{k})$, can be obtained using the eigenfunctions η_{\pm} of σ_x with eigenvalues ± 1 , $\sigma_x \eta_{\pm} = \pm \eta_{\pm}$. Eigenvalues for $H(\mathbf{k})$ are $\nu_{\pm} = H_0 \mp r_k$ and the corresponding eigenfunctions $\psi_{\pm} = U^\dagger \eta_{\pm}$ with the

conventional, or Euclidean, normalization $\psi_\pm^\dagger \psi_\pm = 1$ using unit matrix as the metric for inner product.

However, spin-wave eigenvalue is not the eigenvalue of $H(\mathbf{k})$: Due to the noncommutativity between σ_z and $\sigma_{x,y}$, $H(\mathbf{k})$ and σ_z cannot have simultaneous eigenfunctions. Luckily, as the rotation matrix U still commutes with σ_z , the dispersion relation for spin wave is simple to obtain: $\sigma_z H' = \lambda_k V \sigma_z V^{-1}$, where $\lambda_k = (H_0^2 - r_k^2)^{1/2}$ is positive, can be diagonalized by a symmetric matrix $V = \exp(\sigma_x \beta_k)$ with the angle β_k given by $\tanh 2\beta_k = r_k/H_0$ which, although is real itself, is an imaginary rotation angle in spinor space. λ_k here is just the geometric mean of the two eigenvalues of $H(\mathbf{k})$, $\lambda(k) = \sqrt{\nu_+ \nu_-}$, which is a special feature in \mathbf{k} -space. Due to its dependence on $k_{x,y}^2$ only, λ_k is parity degenerate and states with definite parity can be constructed as the linear combination $\psi \pm \bar{\psi}$, where $\bar{\psi}$ is the wave function after inversion. The only problem for this construction of states with definite parity is associated with the presence of G_{12} , which breaks the 1D inversion symmetries along x and y and hence the inversion symmetry of $H(\mathbf{k})$, albeit λ_k is still invariant under 1D inversions. Spin-wave eigenfrequency can be either positive or negative, $\omega_\pm = \pm \lambda_k$. Actually, the negative frequency branch of the spin-wave spectrum is related to the positive branch by the particle-hole symmetry, and the negative branch is needed to extract m_1 and m_2 as was aforementioned just below Eq (4). Spin-wave eigenfunction is $\psi_\pm = \exp(-i\sigma_z \alpha_k) \exp(\sigma_x \beta_k) \xi_\pm$ with the normalization $\psi_\pm^\dagger \sigma_z \psi_\pm = \pm 1$ using σ_z as the metric, similar to the Minkowski metric in special relativity. ξ_\pm are eigenvectors of σ_z , $\sigma_z \xi_\pm = \pm \xi_\pm$. Due to the non-positive-definite metric σ_z , the inner product of ψ_i^\dagger and ψ_i is not always positive. From the relation $V \sigma_z V^\dagger = \sigma_z$, we can see why we need to use σ_z to normalize the eigenfunction. Another benefit of using the metric σ_z is that the Hermiticity of $H(\mathbf{k})$ ensures that the eigenvalue of $\sigma_z H(\mathbf{k})$ is real²⁰.

An interesting feature of the dipolar interaction can be appreciated by writing out explicitly the Hamiltonian for $\hat{h}_a = \hat{z}$,

$$H(\mathbf{k}) = H_0 + \frac{\sigma_x}{2}(h_b + f_k \cos 2\varphi) + \frac{\sigma_y}{2}f_k \sin 2\varphi \quad (5)$$

where $H_0 = h_0 + h_c - 1 + h_e k^2 - (h_b - f_k)/2$ and $G_+(k) = f_k$, $G_-(k) = f_k \cos 2\varphi$, and $2G_{xy}(k) = f_k \sin 2\varphi$ have been used. Angle φ defines the propagation direction of spin wave, $\tan \varphi = k_y/k_x$. This Hamiltonian resembles that of an electron moving in a uniform electric potential H_0 and a magnetic field $\propto \hat{x}(h_b + f_k \cos 2\varphi) + \hat{y}f_k \sin 2\varphi$, which can be viewed as the effective field of an artificial Rashba spin-orbit interaction $\boldsymbol{\sigma} \cdot (\mathbf{p} \times \hat{z})$ with effective

momentum $\mathbf{p} = \hat{y}(h_b + f_k \cos 2\varphi) - \hat{x}f_k \sin 2\varphi$. In the case of restored in-plane isotropy, $h_b = 0$, only the ubiquitous dipolar field contributes to the spin-orbit coupling for magnons. In the limit $k \rightarrow 0$, $\mathbf{p} \rightarrow (\hat{y} \cos 2\varphi - \hat{x} \sin 2\varphi)tk + \hat{y}h_b$, making the analogy almost perfect for the \mathbf{k} -dependent part of \mathbf{p} , except for the angle 2φ , which should be φ for momentum \mathbf{k} . For large k , the effective spin-orbit field saturates to $\hat{x}(h_b + \cos 2\varphi) + \hat{y} \sin 2\varphi$. As a consequence of the appearance of the artificial Rashba spin-orbit field, a minimum of ω at finite \mathbf{k} will usually develop, similar to the corresponding shifted dispersion relation to electrons under the influence of authentic Rashba interaction^{21–23}.

The origin of the angle 2φ rather than the usual φ can be traced back to the rotation of φ in the spinor space, instead of the usual 3D coordinate space. This is obvious if the unitary rotation by angle φ in the spinor space is performed explicitly as $U^\dagger \sigma_x U = \sigma_x \cos 2\varphi + \sigma_y \sin 2\varphi$ with $U = \exp(i\varphi \sigma_z)$. This doubling in rotation angle is just a manifestation of the two-fold covering of SO(3) by SU(2).

VI. SPIN WAVE IN A WAVEGUIDE

For a waveguide along x , spin wave should have the form $\psi \propto \exp[i(\omega t + k_x x)]$, and the corresponding eigenequation for ω reads $\omega \sigma_z \psi = H(k_x) * \psi$, the analytical solution of which is difficult. We solved it numerically by expanding the wave function into a Fourier series and then diagonalizing the truncated secular matrix to obtain the discrete eigenvalue ω_i and wave function ψ_i . In the expansion of wave function, we used the quantized $wk_y = \pm n_y \pi$, $n_y = 0, 1, 2, \dots$ for positive y -parity states in accordance with the free, or von Neumann, exchange boundary condition $\partial\psi/\partial y = 0$ at $y = \pm w$. Numerically, only one n_y contributes dominantly to ψ_i in k_y -space, and we will use the corresponding n_y with a superscript denoting the y -parity to label the spin-wave frequency bands, unless otherwise stated. Only positive ω_i will be considered, as the negative ω_i are related to the positive ω_i through the particle-hole symmetry. The normalization of wave function is $\langle \psi_i | \sigma_z | \psi_j \rangle = \pm \delta_{ij}$. For the fixed, or Dirichlet, boundary condition $\psi = 0$ at $y = \pm w$, the same set of k_y can also be used for the expansion of wave function, but the resulted states' parity will be reversed, $n^\pm \rightarrow n^\mp$. The n^\pm states with reversed parity for a specific n are slightly different in frequency, although they are degenerate in frequency in an extended film. The monolayer thickness was set to $2t = 1$ nm, which is slightly larger than the actual c value, and the waveguide width was

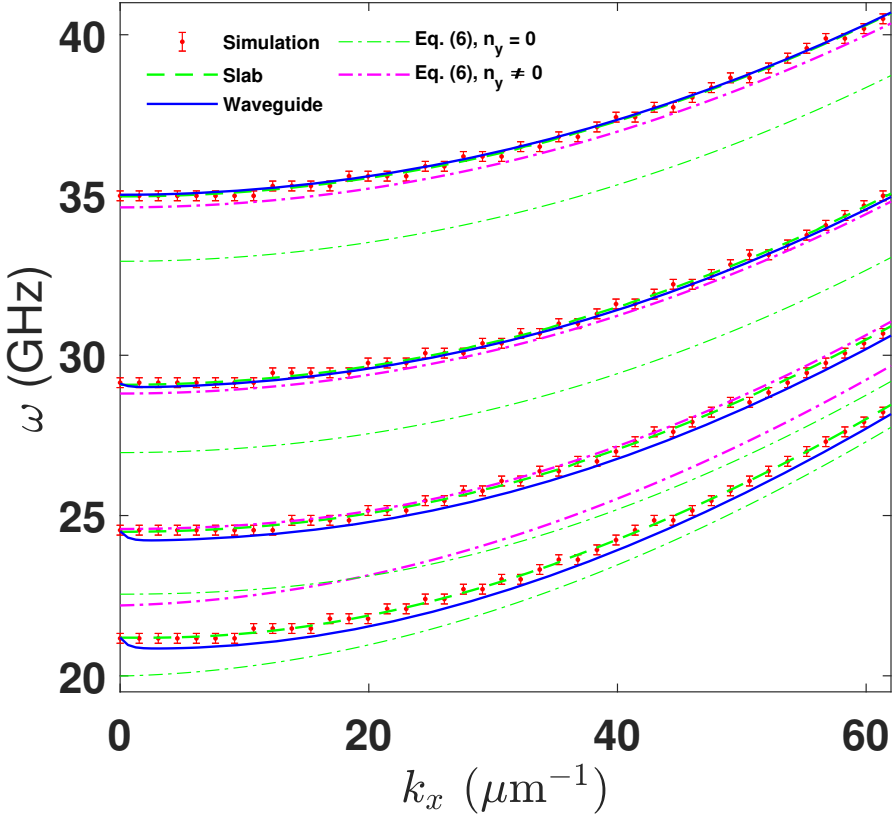


FIG. 3. n^+ spin-wave bands ($n = 0, 1, 2, 3$ from bottom to top) with field $\mu_0 H_a = 0.7$ T along \hat{z} in a waveguide (solid lines) or a slab obtained from calculation (dashed lines) and micromagnetic simulation using OOMMF (symbols). Thick and thin dash-dotted lines correspond to Eq. (6) with $n_y \neq 0$ and $n_y = 0$, respectively. The error bar corresponds to the frequency resolution of the micromagnetic simulation.

chosen to be $2w = 256$ nm.

Figs. 3 shows the n^+ bands obtained by numerically diagonalizing $\sigma_z H$ with $\hat{h}_a = \hat{z}$. According to Table I, the dispersion relation for an extended film is explicitly

$$\omega^2 = (h_0 + k^2 + G_{xx})(h_0 - h_b + k^2 + G_{yy}) \quad (6)$$

where $h_0 = h_a + h_c - 1$, corresponding to the static demagnetization factor $d_0 = n_z = G_{zz}(k = 0) = 1$. For the film thickness of $2t = 1$ nm considered here, we had checked that the dispersion relation obtained by solving the boundary problem using linear superposition of eigenfunctions^{25,26} is numerically identical to Eq. (6)²⁷. As we had deliberately chosen $h_0 > h_b$ to ensure the stability of the ground state, the usual manifestation of the spin-wave

spin-orbit coupling, $d\omega/dk_x < 0$ which requires $h_b \cos^2 \varphi > h_0$ for a fixed $\varphi \neq \pm\pi/2$ and $f_k \in [0, 1)$, cannot be observed for the dispersion given by Eq. (6). If the presence of boundary only introduces quantized wave vector as discussed in Ref. [24], Eq. (6) should give a good description of the spin-wave bands, all of which should have positive group velocity. However, bands up to 2^+ have negative group velocity around $k_x = 0$ and all the numerical bands have frequency higher than that predicted by Eq. (6). The downward turn of the lower frequency bands are caused by the dynamic dipolar field characterized by G_{zz} . The upward shift in frequency of the numerical bands in comparison to Eq. (6) is due to the static demagnetization factor²⁸ for a waveguide $n_z = 1 - n_y$ where $n_y = 8.76 \times 10^{-3}$ is actually smaller than the value $n_z = 1$ used in Eq. (6). Corresponding to the non-zero n_y , the modified $G_{zz} = n_z - f_k$ and $G_{yy} = n_y + f_k \sin^2 \varphi$ have to be made to satisfy the constraint $(G_{zz} + G_{yy} + G_{xx})(\mathbf{k}) = 1$. A better description of the numerical result can be achieved with this modification: Except for the 0^+ band, all higher n^+ bands can be approximated. The inability to describe the 0^+ band by an effective n_y can be attributed to the sensitivity of long-wavelength wave to the details at the boundary of the potential caused by the static dipolar field. If the wave length is small, the average potential will be determined mainly by the slowly-varying, or bulk, feature of the static potential, hence the description using n_y preforms better for higher n . Although Eq. (6) with $n_y = 0$ agrees poorer with the numerical results, but it describes better the n^- bands with the fixed boundary condition (not shown here). The reason behind this agreement is simply because that, due to the fixed boundary condition, spin wave is pushed away from the boundaries at $y = \pm w$, where the static dipolar field concentrates, as shown in Fig. 2. Hence the effective potential felt by spin wave with fixed boundary condition is similar to that of an extended film, which can be described better by Eq. (6). The frequency splitting between bands with reversed parity, hence also corresponding to different boundary conditions (free or fixed), for specific n can be roughly estimated between bands given in Fig. 3 with two choices for n_y . It is also interesting to note that, although in this case the potential caused by the dipolar field is locally parabolic, thus locally similar to the parabolic potential previously demonstrated to accommodate localized spin wave²⁹, there is no localized state observed in Fig. 3, as the potential roughly scales as the inverse of $1 - cy^2$ with constant $c < 1$, which is not globally parabolic.

When $\hat{h}_a = \hat{y}$, i.e. in the Damon-Eshbach geometry^{31,32}, the obtained energy bands are

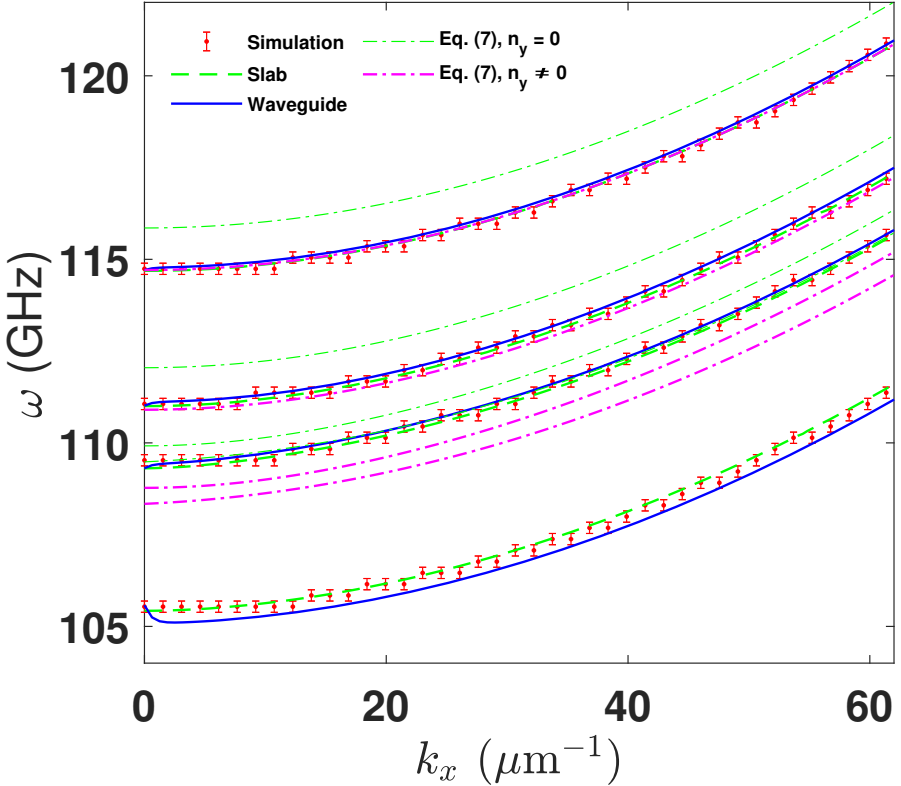


FIG. 4. n^+ spin-wave bands with field $\mu_0 H_a = 0.2$ T along \hat{y} in the notation of Fig. 3. Thick and thin dash-dotted lines correspond to Eq. (7) with $n_y \neq 0$ and $n_y = 0$, respectively. The lowest band is a localized band, while the other bands correspond to $n = 0, 2, 3$ from bottom to top

shown in Fig. 4. In this case, the lowest band is the Damon-Eshbach mode, which is a localized mode (See Sec. VIII). The extended bands start from 0^+ , as usual, but with the 1^+ band missing; So the band just above the second (0^+) band is the 2^+ band. The Damon-Eshbach band is the only band that has a local minimum; Other bands are monotonic functions of k_x . Using Table I, the dispersion curves for an extended filem are given by

$$\omega^2 = (h_0 - h_c + k^2 + G_{zz})(h_0 + k^2 + G_{xx}), \quad (7)$$

which are all above the numerical bands. When the dipolar field is considered using the n_y given above, the static field is reduced to $h_0 = h_a + h_b - n_y$, which clearly shows that the inclusion of n_y will reduce the frequency ω and can explain the reversal of order between the numerical results and Eq. (7) with $n_y = 0$. But the lowering of the frequency by using an average n_y is not enough to explain the numerical result; the lowest band is further below the lowest band predicted by Eq. (7) with $n_y \neq 0$, altough other bands, both calculated

and simulated, agree fairly well with the $n_y \neq 0$ results. One additional feature for the Damon-Eshbach geometry is the reversal of order for the parity doublets with one k_y value: The n^+ (free boundary) state is lower in frequency than its n^- (fixed boundary) partner, while it is the opposite case for $\hat{h}_0 = \hat{z}$. This is caused by the inverted, barrier shape of the static dipolar field, which is a potential well when $\hat{h}_0 = \hat{z}$: As the wave function of the n^+ states does not vanish at the y -boundary due to the von Neumann boundary condition, the n^+ states tend to have a lower frequency than their n^- partners whose wave function vanishes there.

The frequency bands for $\hat{h}_a = \hat{x}$ are given in Fig. 5. There are two $(0^+, 1^+)$ waveguide and one (0^+) slab bands showing negative group velocity in the vicinity of $k_x = 0$. In this configuration, we can easily see from the dispersion relation for an extended film,

$$\omega^2 = (h_0 - h_b + k^2 + G_{yy})(h_0 - h_c + k^2 + G_{zz}), \quad (8)$$

that, with $\varphi = 0$, there is always an interval in k_x where the group velocity is negative, as $h_0 > h_b$ is chosen in our calculation. In this case, as there is no static dipolar field for a waveguide, Eq. (8) with the modified dynamic G_{yy} gives a very good approximation to the numerical result.

VII. SPIN WAVE IN A SLAB

As an ideal, infinitely long, waveguide is difficult to realize experimentally, it is of interest to consider the spin-wave spectrum of a finite slab and to see how it is related to the spectrum of an ideal waveguide. To this aim, we performed theoretical calculation for a slab, similar to the waveguide case shown in Sec. VI. We chose an aspect ratio of $l/w = 64$ with the same width $2w = 256$ nm for the waveguide considered in Sec. VI. When $\hat{h}_a = \hat{z}$, due to the appearance of G_{xy} , P_x and P_y are not exact. But the effect of parity violation is small, and we can still separate states according to their approximate $P_{x,y}$. As the frequency splitting of P_x^\pm states is small, which is mainly caused by the smallness of π/l , we just averaged their values to get one frequency with definite P_y .

One benefit provided by the finite size of the slab is that the same spin-wave spectrum can be investigated by micromagnetic simulation, as an additional check of our theoretical calculation. We used OOMMF³⁰ for this purpose. The simulated geometry is identical to

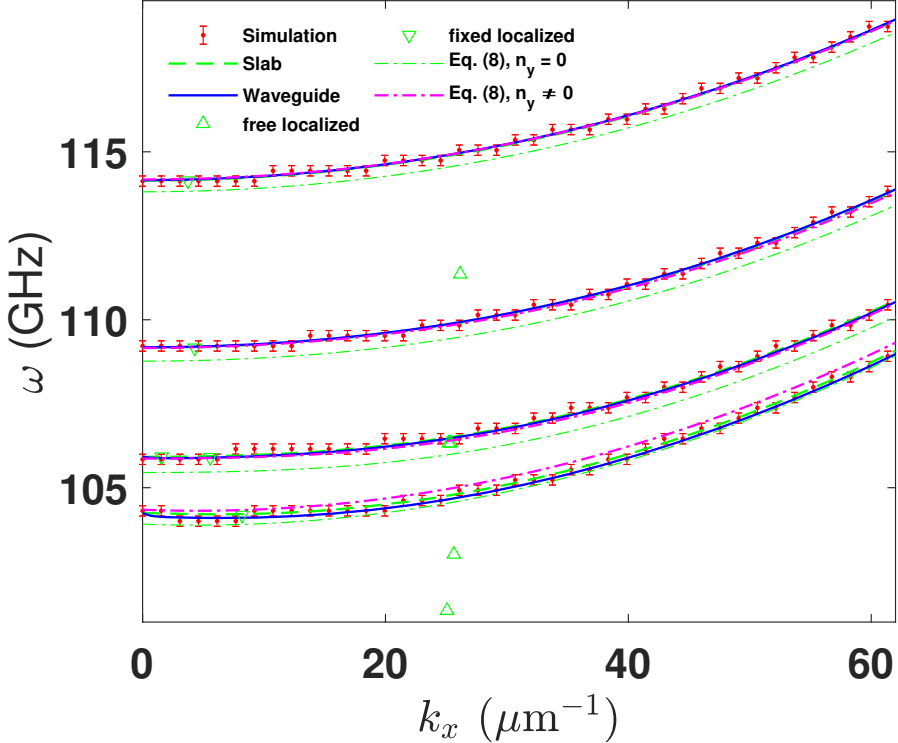


FIG. 5. n^+ spin-wave bands with field $\mu_0 H_a = 0.6$ T along \hat{x} in the notation of Fig. 3. Thick and thin dash-dotted lines correspond to Eq. (8) with $n_y \neq 0$ and $n_y = 0$, respectively. Localized states with positive x -parity for the slab geometry are shown as triangles.

our theoretical calculation, i.e. a monolayer CrSBr with length $2l = 16384\Delta$ and width $2w = 256\Delta$, where $\Delta = 1$ nm is the mesh size, which coincides with the monolayer thickness $2t = \Delta$. Δ used here is smaller than the exchange length, $l_{ex} \sim 4$ nm, calculated using K_d . Comparison simulations were carried out to check that increase of Δ to 4 nm does not change the obtained dispersion relations substantially. A uniform state magnetized along one of three principal crystallographic axes is chosen as the initial state for subsequent time evolution over 1 ns with α set to 1. The obtained state is then minimized by conjugate gradient (CG) method as implemented in OOMMF. The CG minimization is just employed to ensure that the time-evolved state with finite α is still stable when α is set to zero for spin-wave simulation. Spin wave was excited by an oscillating field $h_0 \text{sinc}(\omega_c t_r) \text{sinc}(k_x^c x_r) f_{\pm}(y)$ with $h_0 = 10^2$ A/m and $f_+ = \text{sinc}(k_y^c y_r)$ or $f_- = \text{sinc}(k_y^c y_r/2) \sin(k_y^c y_r/2)$ for P_y^{\pm} spin wave. The oscillating field is perpendicular to the applied field \mathbf{h}_a : When $\hat{h}_a = \hat{z}$, it is parallel to \hat{y} ; otherwise, it is parallel to \hat{z} . $x_r = x - x_0$, $y_r = y - y_0$ and $t_r = t - t_0$ are used to peak

the excitation field at the centre of both time and space. The cut-off frequency is $\omega_c/2\pi = 25$ GHz, and the cut-off wave numbers are $k_x^c = 80 \pi/l$ and $k_y^c = 12 \pi/w$. A square-wave distribution in both frequency and \mathbf{k} was emulated by the sinc function, $\text{sinc}(x) = \sin(x)/x$, while f_- was used to approximate an antisymmetric uniform distribution in k_y up to k_y^c . Once the ground state was determined, the whole system was evolved in time with the oscillating field turned on for 20.48 ns with zero damping, outputting snapshots of magnetization state every 20 ps. Distribution of the spin-wave amplitude in ω and k_x was obtained from fast Fourier transform of the output snapshots with respect to both t and x , at $y = \pm(w - \Delta/2)$ ($\pm\Delta/2$) for the P_y^+ (P_y^-) modes.

Qualitative, the simulated ground state with $\hat{h}_a = \hat{x}$ or \hat{y} is different from that with $\hat{h}_a = \hat{z}$. For the field $\mu_0 h_a = 0.7$ T applied along \hat{z} , the ground state is uniformly magnetized along \hat{z} , as in this case, the static dipolar field is simply antiparallel to \mathbf{h}_a due to the block-diagonal structure of G_{ij} . However, a uniform state magnetized in-plane along either \hat{x} or \hat{y} will become unstable, as the non-vanishing G_{xy} will induce an additional dipolar field component orthogonal to the uniform magnetization, and the ground state changes to the so-called 'flower state'³⁴ with curling around the four corners when $\hat{h}_a = \hat{x}$ or \hat{y} . From the study of spin wave in magnetization textures¹⁸ such as skyrmions⁶ and domain walls³⁵, it is well known that magnetization textures will induce an emergent gauge field for magnons, further complicating the spin-wave dynamics. The correction induced by the emergent gauge field was neglected in our calculation of the dispersion relation simply because its contribution to the Hamiltonian matrix is negligible²⁷. As aforementioned, the parity-violation G_{xy} is static and its effect on spin wave is mediated through the induced magnetization texture in the ground state, which is not symmetric under 1D inversion. But the non-uniformity is extremely weak since the applied in-plane field is large; The effect of G_{xy} is mostly suppressed by \mathbf{h}_a . When $\hat{h}_a = \hat{z}$, the situation is different: G_{xy} acts as a dynamic dipolar field rather than being static and it is explicitly included in H .

The simulated bands are plotted together with the calculated bands in Figs. 3, 4, and 5. They agree with each other within the simulation uncertainty. Except for the lowest one or two bands, the band structure for all three directions of \mathbf{h}_a can be better described by non-zero in-plane demagnetization factors, similar to Sec. VI, but with a slightly different²⁸ $n_y = 8.74 \times 10^{-3}$ and non-zero $n_x = 1.31 \times 10^{-4}$. The additional modification to the Green function corresponding to n_x is $G_{xx} = n_x + f_k \cos^2 \varphi$. As the difference in value between

n_y and n_x for the slab geometry considered here and the waveguide geometry in Sec. VI is small and the resulted change is well within the plotted line thickness, we used the values give here even for the waveguide case in Sec. VI.

The overall agreement between slab and waveguide spin-wave bands is reasonable in Fig. 3, especially for bands with $n > 0$. However, there are discrepancies at small $|k_x|$, where the 0^+ waveguide band has a deeper and wider dip but the corresponding band given by simulation is rather shallow and narrow. Until the 2^+ band, the waveguide bands still have a local minimum. This demonstrates clearly that the aspect ratio used in the simulation, $l/w = 64$, is still not large enough to capture the physics for an infinitely-long waveguide. This feature is shared by the other two cases: There is only one (0^+) slab band showing negative group velocity in the vicinity of $k_x = 0$ for $\hat{h}_a = \hat{x}$, while the group velocity of all slab bands is positive with $\hat{h}_a = \hat{y}$.

An outstanding feature of the slab geometry is the appearance of localized states in band gap of the calculated spectrum with $\hat{h}_a = \hat{x}$. They are localized about the two x -edges at $x = \pm l$. Those localized states are not observed in the simulated spectrum, possibly due to their localized character and a correspondingly small excitation efficiency in response to the applied field. A localized field can be used to excite them in simulation²⁷. Experimentally, those localized states may be observed by Brillouin light scattering³³.

VIII. ORIGIN OF THE DAMON-ESHBACH MODE

The lowest band in Fig. 4, which lies below the lowest dispersion curve for an infinite film, corresponds to the Damon-Eshbach mode^{31,32}, which is localized around the two edges at $y = \pm w$, as demonstrated by the spin-wave amplitude distribution shown in Fig. 6. Although it was discovered more than sixty years ago, its physical origin is still under debate. Inspired by its rather robust feature against back scattering, the authors of Ref. [36] suggested that the Damon-Eshbach mode is actually the edge mode determined by the topological winding number around four vortices that are time-reversal invariant in the reciprocal space. What we found is in stark contradiction with this topological origin: The existence of the Damon-Eshbach mode is simply caused by the confining potential provided by the static dipolar field, which acts as a potential in the BdG formulation of spin-wave equation of motion and is plotted in Fig. 2. The barrier shape of the dipole potential

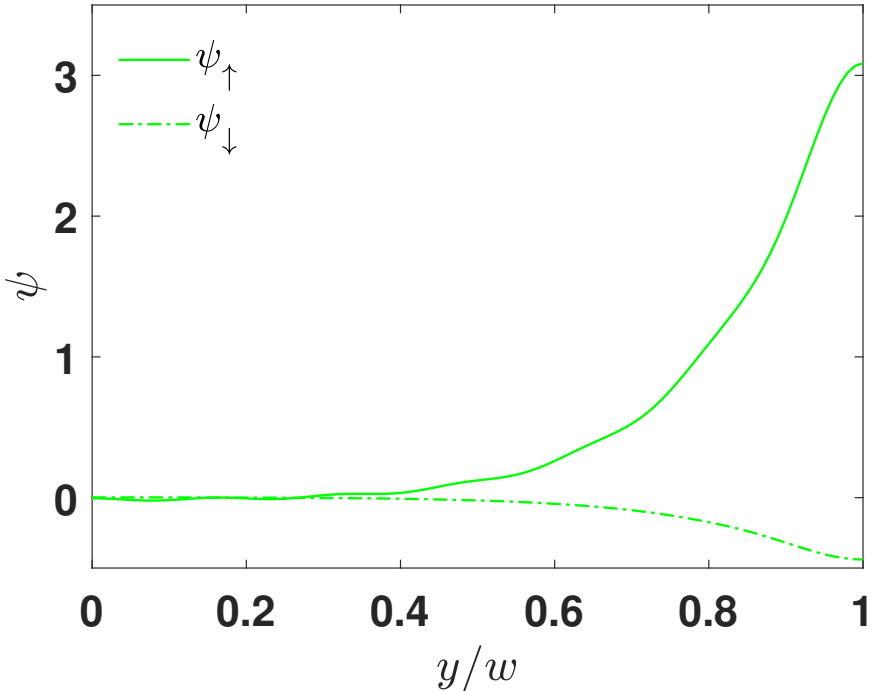


FIG. 6. Damon-Eshbach spin-wave wave function at $k_x = 0$.

indicates that the edges of a waveguide are more energetically favourable for spin wave to dwell on, just by reducing the total spin-wave energy in comparison to spreading around the centre of a waveguide, where the potential has a maximum.

In the usual bulk-boundary correspondence of topology, the appearance of topological edge modes localized around a topology defect also relies on the presence of interactions that interpolate continuously across the defect. However, according to Eq. (1), the static dipolar potential is not continuous across the waveguide edges, as required by the continuity of the **B** field and shown in Fig. 2. The discontinuity of the potential indicates that the Damon-Eshbach mode is not derived from the usual bulk-boundary correspondence of topology.

There are several possible reasons why the topological prediction does not realise in the case of exchange-dipole spin wave in a ferromagnetic waveguide. The most import one is the long-range characteristic of dipolar interaction, which makes the Hamiltonian a non-analytic function in both coordinate²⁷ and reciprocal spaces. The aforementioned discontinuity in Fig. 2 is just a manifestation of this point in 1D coordinate space. The ambiguity in defining a continuous Hamiltonian in reciprocal space, as already pointed out in Ref. [36], is

another manifestation. For consideration of topology, usually the Hamiltonian needs to be a continuous mapping between topological spaces³⁷. Secondly, the classification of topology³⁷ according to the symmetry of the Hamiltonian for Fermions which obey anti-commutation relation is applied to spin wave³⁶, the quanta of which, magnons, should be Bosons and obey the commutation relation. Different statistics of Fermions and Bosons require different symmetry constraints for the single-particle Hamiltonian. Bosonic statistics will definitely modify the outcome of Ref. [36], which identified the topology of spin-wave single-particle Hamiltonian as class CI with time-reversal, particle-hole, and chiral symmetries³⁷. Even this classification of topology was controversial: By considering the Krein structure of the spin-wave BdG equation, Ref. [19] claimed that the topology class of spin wave is actually A with no symmetry at all³⁷, rather than CI. The classification of topology class A does not depend on the particle statistics, as it has no additional symmetry and hence no symmetry constraints need be considered. Last but not least, it is recently pointed out that bulk band topology does not necessarily lead to topologically protected edge states with codimension 1^{38,39}.

IX. CONCLUSION

Spin wave in monolayer CrSBr waveguides with field applied along all three principal crystallographic axes was investigated by a BdG formulation of the linearised LLG equation. Due to the spinor structure of the BdG equation and inversion symmetry, spin-wave eigenfrequencies form almost degenerate doublets with distinct parity, corresponding to different boundary conditions. Due to magnetostatic charge accumulation at the waveguide edges, static dipolar field acts as a confining potential for spin wave and localization of spin wave at the edges gives rise to the Damon-Eshbach mode. More localized states around the short edges of a ferromagnetic slab can be brought about by static dipolar field when the external field is applied along the long edges. Dynamic dipolar field couples the momentum and spin degrees of freedom of spin wave, resulting in spin-orbit coupling for magnons which is similar to that for electrons. The magnonic spin-orbit coupling is usually manifested by a negative group velocity for spin wave with small k_x ; spin wave inside this region of k_x is commonly dubbed backward propagating.

ACKNOWLEDGMENTS

The work was supported by the project Quantum Materials for Sustainable Technologies (QM4ST), no. CZ.02.01.01/00/22_008/0004572, funded by the MEYS and co-funded by the EU.

* daowei.wang@matfyz.cuni.cz

† jana.vejpravova@matfyz.cuni.cz

- ¹ K. S. Novoselov, A. K. Geim, S. V. Morozov, D. Jiang, Y. Zhang, S. V. Dubonos, I. V. Grigorieva, and A. A. Firsov, Electric field effect in atomically thin carbon films, *Science* 306, 666 (2004).
- ² K. S. Novoselov, Z. Jiang, Y. Zhang, S. V. Morozov, H. L. Stormer, U. Zeitler, J. C. Maan, G. S. Boebinger, P. Kim, and A. K. Geim, Room-temperature quantum hall effect in Graphene, *Science* 315, 1379 (2007).
- ³ B. Huang, G. Clark, E. Navarro-Moratalla, D. R. Klein, R. Cheng, K. L. Seyler, D. Zhong, E. Schmidgall, M. A. McGuire, D. H. Cobden, W. Yao, D. Xiao, P. Jarillo-Herrero, and X. Xu, Layer-dependent ferromagnetism in a van der Waals crystal down to the monolayer Limit, *Nature* 546, 270 (2017).
- ⁴ K. Lee, A. H. Dismukes, E. J. Telford, R. A. Wiscons, J. Wang, X. Xu, C. Nuckolls, C. R. Dean, X. Roy, X. Zhu, Magnetic order and symmetry in the 2D semiconductor CrSBr, *Nano Lett.* 21, 3511 (2021).
- ⁵ M. E. Ziebel, M. L. Feuer, J. Cox, X. Zhu, C. R. Dean, and X. Roy, CrSBr: An air-stable, two-dimensional magnetic semiconductor, *Nano Lett.* 24, 4319 (2024).
- ⁶ D. Wang, H.-B. Braun, and Y. Zhou, Dynamical mass generation for ferromagnetic skyrmions in two dimensions, *J. Magn. Magn. Mater.* 564, 170062 (2022).
- ⁷ A. Scheie, M. Ziebel, D. G. Chica, Y. J. Bae, X. Wang, A. I. Kolesnikov, X. Zhu, and X. Roy, Spin waves and magnetic exchange Hamiltonian in CrSBr, *Adv. Sci.* 9, 2202467 (2022).
- ⁸ T. M. J. Cham, S. Karimeddiny, A. H. Dismukes, X. Roy, D. C. Ralph, and Y. K. Luo, Anisotropic gigahertz antiferromagnetic resonances of the easy-axis van der Waals antiferromagnet CrSBr, *Nano Lett.* 22, 6716 (2022).

⁹ R. den Teuling, R. Das, A. V. Bondarenko, E. V. Tartakovskaya, G. E. W. Bauer, and Y. M. Blanter, Spin waves in the bilayer van der Waals magnet CrSBr, *Phy. Rev. B* 112, 144442 (2025).

¹⁰ H. Xu, N. Jiang, H. Chen, Y. Chen, T. Wu, Y. Cui, Y. Wu, Z. Sheng, Z. Sun, J. Xu, Q. Mi, S. Wu, W. Yu, and Y. Wu, Magnetostatic effect on spin dynamics properties in the antiferromagnetic van der Waals material CrSBr, *Phys. Rev. B* 111, 024410 (2025).

¹¹ K. Yang, G. Wang, L. Liu, D. Lu, and H. Wu, Triaxial magnetic anisotropy in the two-dimensional ferromagnetic semiconductor CrSBr, *Phys. Rev. B* 104, 144416 (2021).

¹² O. Göser, W. Paul, H. G. Kahle, Magnetic properties of CrSBr, *J. Magn. Magn. Mater.* 92, 129 (1990).

¹³ C. W. Cho, A. Pawbake, N. Aubergier, A. L. Barra, K. Mosina, Z. Sofer, M. E. Zhitomirsky, C. Faugeras, and B. A. Piot, Microscopic parameters of the van der Waals CrSBr antiferromagnet from microwave absorption experiments, *Phys. Rev. B* 107, 094403 (2023).

¹⁴ L. Exl, D. Suess, and T. Schrefl, Micromagnetism in *Handbook of Magnetism and Magnetic Materials*, J. M. D. Coey and S. S. P. Parkin (eds), Springer Cham, 2021. (<https://doi.org/10.1007/978-3-030-63210-6>)

¹⁵ F. N. Rybakov, N. S. Kiselev, A. B. Borisov, L. Döring, C. Melcher, S. Blügel, Magnetic hopfions in solids, *APL Mater.* 10, 111113 (2022).

¹⁶ K. Y. Guslienko and A. N. Slavin, Magnetostatic Green's functions for the description of spin waves in finite rectangular magnetic dots and stripes, *J. Magn. Magn. Mater.* 323, 2418 (2011).

¹⁷ T. L. Gilbert, A phenomenological theory of damping in ferromagnetic materials, *IEEE Trans. Mag.* 40, 3443 (2004).

¹⁸ V. K. Dugaev, P. Bruno, B. Canals, and C. Lacroix,, Berry phase of magnons in textured ferromagnets, *Phys. Rev. B* 72, 024456 (2005).

¹⁹ M. Lein and K. Sato, Krein-Schrödinger formalism of bosonic Bogoliubov–de Gennes and certain classical systems and their topological classification, *Phys. Rev. B* 100, 075414 (2019).

²⁰ A. Mostafazadeh, Pseudo-Hermiticity versus PT symmetry: The necessary condition for the reality of the spectrum of a non-Hermitian Hamiltonian, *J. Math. Phys.* 43, 205 (2002).

²¹ D. Wang and Yan Zhou, Scaling of the Rashba spin-orbit torque in magnetic domain walls, *J. Magn. Magn. Mater.* 493, 165694 (2020).

²² D. Wang and Y. Zhou, Topological damping Rashba spin-orbit torque in ballistic magnetic domain walls, *Phys. Rev. B* 101, 020410 (2020).

²³ D. Wang and Y. Zhou, Algebraic decay of the nonadiabaticity arising through chiral spin transfer torque in magnetic domain walls with Rashba spin-orbit interaction, *Phys. Rev. B* 101, 184428 (2020).

²⁴ K. Yu. Guslienko, S. O. Demokritov, B. Hillebrands, and A. N. Slavin, Effective dipolar boundary conditions for dynamic magnetization in thin magnetic stripes, *Phys. Rev. B* 66, 132402 (2002).

²⁵ R. E. De Wames and T. Wolfram, Dipole-exchange spin waves in ferromagnetic films, *J. Appl. Phys.* 41, 987 (1970).

²⁶ B. Hillebrands, Spin-wave calculations for multilayered structures, *Phys. Rev. B* 41, 530 (1990).

²⁷ See Supplemental Material at <http://link.aps.org/xxx> for (a) spin-wave dispersion obtained from boundary condition, (b) effect of magnetization curling on spin wave, (c) negative y -parity bands, (d) static demagnetization field of a slab, and (e) spin-wave distribution of the localized states.

²⁸ A. Aharoni, Demagnetizing factors for rectangular ferromagnetic prisms, *J. Appl. Phys.* 83, 3432 (1998).

²⁹ E. V. Tartakovskaya, M. Pardavi-Horvath, and R. D. McMichael, Spin-wave localization in tangentially magnetized films, *Phys. Rev. B* 93, 214436 (2016).

³⁰ OOMMF User's Guide, Version 2.0b0, M. J. Donahue and D. G. Porter, National Institute of Standards and Technology, Gaithersburg, MD. DOI: 10.18434/T4/1502495.

³¹ J. R. Eshbach and R. W. Damon, Surface magnetostatic modes and surface spin waves, *Phys. Rev.* 118, 1208 (1960).

³² R. W. Damon and J. R. Eshbach, Magnetostatic modes of a ferromagnet slab, *J. Phys. Chem. Solids* 19, 308 (1961).

³³ M. G. Copus, T. Hula, C. Heins, L. Flacke, M. Weiler, K. Schultheiss, H. Schultheiss, and R. E. Camley, Generation of localized, half-frequency spin waves in micron sized ferromagnetic stripes: Experiments and simulations, *Appl. Phys. Lett.* 124, 192401 (2024).

³⁴ W. Rave, K. Fabian, and A. Hubert, Magnetic states of small cubic particles with uniaxial anisotropy, *J. Magn. Magn. Mater.* 190, 332 (1998); See also the μ MAG Standard Problem #3 at <https://www.ctcms.nist.gov/mumag/mumag.org.html>.

³⁵ D. Wang, Y. Zhou, Z.-X. Li, Y. Nie, X.-G. Wang and G.-H. Guo, Magnonic band structure of domain wall magnonic crystals, *IEEE Trans. Magn.* 53, 1300110 (2017).

³⁶ K. Yamamoto, G. C. Thiang, P. Pirro, K.-W. Kim, K. Everschor-Sitte, and E. Saitoh, Topological characterization of classical waves: The topological origin of magnetostatic surface spin waves, *Phys. Rev. Lett.* 122, 217201 (2019).

³⁷ C.-K. Chiu, J. C. Y. Teo, A. P. Schnyder, and S. Ryu, Classification of topological quantum matter with symmetries, *Rev. Mod. Phys.* 88, 035005 (2016).

³⁸ S. Xu, Y. Wang, and R. Agarwal, Reply to Comment on: Absence of topological protection of the interface states in \mathbb{Z}_2 photonic crystals, *Phys. Rev. Lett.* 134, 099302 (2025).

³⁹ S. Xu, Y. Wang, and R. Agarwal, Absence of topological protection of the interface states in \mathbb{Z}_2 photonic crystals, *Phys. Rev. Lett.* 131, 053802 (2023).

Supplemental Material

I. SPIN WAVE DISPERSION FROM BOUNDARY CONDITION

In the magneto-static approximation, the two magnetic Maxwell equations become $\nabla \cdot \mathbf{B} = 0, \nabla \times \mathbf{H} = 0$, as the mutual excitation between the magnetic and electric fields is neglected. With the definition of a scalar potential, $\mathbf{H} = -\nabla\phi$, the equation for ϕ is $\nabla^2\phi = \nabla \cdot \mathbf{m}$. For spin wave $\propto \exp i(k \cdot \mathbf{x} + \omega t)$, $k^2\phi = -i\mathbf{k} \cdot \mathbf{m}_1$. $\mathbf{h} = -\mathbf{k}\mathbf{k} \cdot \mathbf{m}_1/k^2$. The singularity at $k^2 = 0$ is caused by the dispersion of the electromagnetic field in the magneto-static approximation, $k^2 = \omega^2/c^2 = 0$, which is equivalent to $c \rightarrow \infty$. Effectively, the dynamic dipolar field can be expressed through a Green function $G_{ij}(k) = k_i k_j / k^2$, $i, j = 1, 2$. Using Table I and results of Sec. V in the main text, the spin-wave frequency is given by

$$\omega^2 = (h_0 + k^2 - h_1 + G_{11})(h_0 + k^2 - h_2 + G_{22}) - G_{12}^2. \quad (\text{S1})$$

Due to the cancellation enabled by the relation $G_{12}^2 = G_{11}G_{22}$, the equation for k^2 is of order three for fixed ω^2 and k^2 has three roots in the complex domain, one being real and the other two being complex conjugate to each other. We can label the k_z corresponding to the three k^2 roots as k_z^i , $i = 1$ to 6. Inside the infinite film ($z \in [-t, t]$), ϕ , m_1 and m_2 can be expressed as the linear superposition of the six eigenmodes with different k_z^i ,

$$\phi = c_i e^{ik_i z} e^{i(\omega t + k_y y)}, m_1 = a_i e^{ik_i z} e^{i(\omega t + k_y y)}, m_2 = b_i e^{ik_i z} e^{i(\omega t + k_y y)}.$$

Coefficients a_i and b_i for each mode i are related to c_i through the equation of motion for spin wave as

$$\frac{a_i}{c_i} = \frac{i(h_0 + k^2 - h_2)k_1 - \omega k_2}{D}, \frac{b_i}{c_i} = \frac{\omega k_1 + i(h_0 + k^2 - h_1)k_2}{D}, \quad (\text{S2})$$

where the denominator $D = \omega^2 - (h_0 + k^2 - h_1)(h_0 + k^2 - h_2)$, the pole of which gives the spin-wave dispersion relation without considering the dynamic dipolar field. Above ($z \in (t, \infty)$) and below ($z \in (-\infty, -t)$), the scalar potential is given by $\phi = \phi_{\pm} e^{\mp z k_p} e^{i(\omega t + k_y y)}$. At the boundaries $z = \pm t$, the continuity of the normal component of \mathbf{B} and the tangential component of \mathbf{H} has to be satisfied, in addition to the boundary condition for magnetization $\partial_z \mathbf{m}_1 = 0$, which gives

$$\begin{aligned} z = -t, \phi_- e^{ik_2 z} &= c_i e^{ik_i z}, ik_2 \phi_- e^{ik_2 z} = (ic_i k_i - b_i) e^{ik_i z}, b_i k_i e^{ik_i z} = 0, a_i k_i e^{ik_i z} = 0. \\ z = t, \phi_+ e^{ik_1 z} &= c_i e^{ik_i z}, ik_1 \phi_+ e^{ik_1 z} = (ic_i k_i - b_i) e^{ik_i z}, b_i k_i e^{ik_i z} = 0, a_i k_i e^{ik_i z} = 0. \end{aligned} \quad (\text{S3})$$

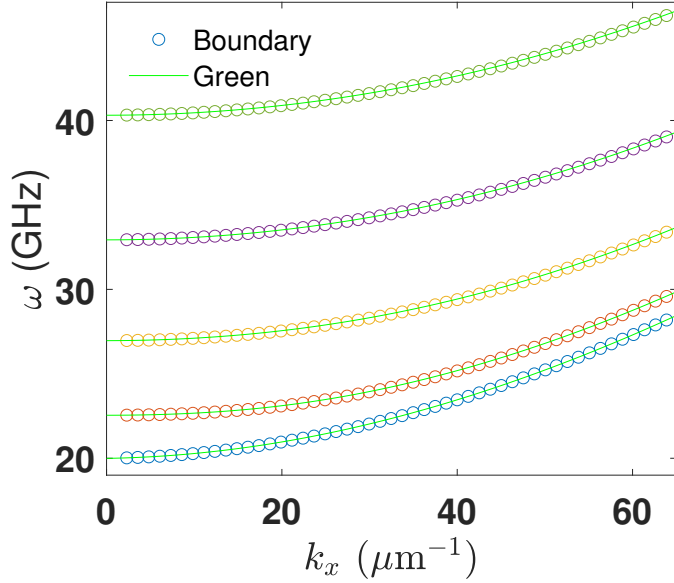


FIG. S1. Spin-wave dispersion curves obtained from boundary condition and Green function with $\hat{h}_a = \hat{z}$.

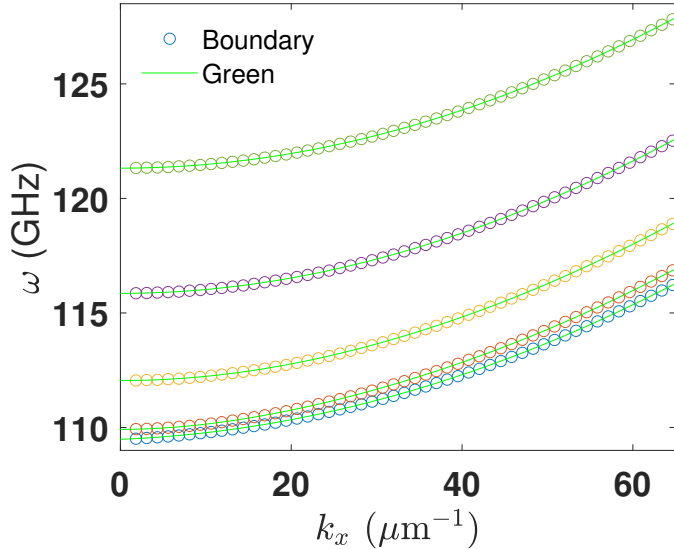


FIG. S2. Spin-wave dispersion curves obtained from boundary condition and Green function with $\hat{h}_a = \hat{y}$.

Setting the determinant of the secular matrix obtained from the coefficients of the linear system of equations gives the spin-wave dispersion relation. The results are shown in Figs. S1, S2, and S3. It can be seen that both approaches give almost identical results for monolayer CrSBr.

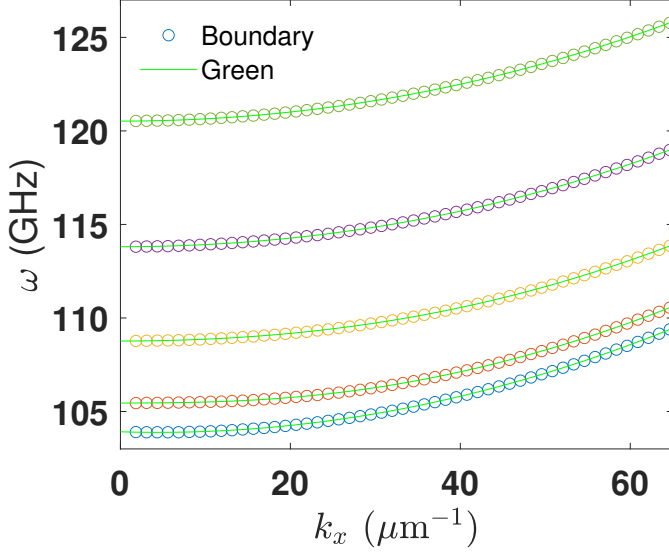


FIG. S3. Spin-wave dispersion curves obtained from boundary condition and Green function with $\hat{h}_a = \hat{x}$.

II. HAMILTONIAN WITH IN-PLANE MAGNETIZATION CURLING

When $\hat{h}_a = \hat{x}$, the Hamiltonian components are

$$H_0 = h_a \cos \theta + \frac{3}{2} h_b \sin^2 \theta - \frac{h_b + h_c + (\nabla \theta)^2}{2} - \nabla^2 - d_0 + \frac{G_{11} + G_{zz*}}{2},$$

$$2H_1 = h_c - h_b \cos^2 \theta + (\nabla \theta)^2 + G_{11} - G_{zz*}, \quad (S4)$$

where the static dipolar field $d_0 = [(G_{xx} * \cos \theta) + (G_{xy} * \sin \theta)] \cos \theta + [(G_{yy} * \sin \theta) + (G_{xy} * \cos \theta)] \sin \theta$ and $G_{11} = \cos \theta (G_{yy} * \cos \theta - G_{xy} * \sin \theta) + \sin \theta (G_{xx} * \sin \theta - G_{xy} * \cos \theta)$ in the local coordinate frame where the local magnetization is along \hat{e}_3 . Correspondingly, when $\hat{h}_a = \hat{y}$,

$$H_0 = h_a \cos \theta + \frac{3}{2} h_b \cos^2 \theta - \frac{h_b + h_c + (\nabla \theta)^2}{2} - \nabla^2 - d_0 + \frac{G_{zz*} + G_{22}}{2},$$

$$2H_1 = h_b \sin^2 \theta - h_c - (\nabla \theta)^2 + G_{zz*} - G_{22}. \quad (S5)$$

$d_0 = [(G_{yy} * \cos \theta) - (G_{xy} * \sin \theta)] \cos \theta + [(G_{xx} * \sin \theta) - (G_{xy} * \cos \theta)] \sin \theta$, and $G_{22} = \cos \theta (G_{xx} * \cos \theta + G_{xy} * \sin \theta) + \sin \theta (G_{yy} * \sin \theta + G_{xy} * \cos \theta)$. In both cases, the non-uniform distribution of magnetization is characterized by the angle θ which measures the in-plane rotation from \mathbf{h}_a to \mathbf{m}_0 . θ is of the order of 10^{-2} or smaller for values of h_a considered in the main text.

In comparison to the uniform case by setting θ to zero, we can see that the correction induced by in-plane magnetization curling is proportional to θ^2 . Using the texture profiles simulated from OOMMF, we computed the correction's distribution over the prism, excluding the dynamic dipolar field (G_{\pm}) contribution. It was found that the correction to both H_0 and H_1 is peaked around the four corners with magnitude of the order of at most 10^{-3} , which is what can be expected as θ is not zero only around the corners. Integration of the distribution over the prism region is used to estimate the correction to the Hamiltonian matrix. The correction is only of the order of 10^{-7} for H_0 , which is far below the resolution of frequency 3.3×10^{-3} used in simulation. It is even one order smaller for H_1 . Corrections with non-zero momentum transfer \mathbf{k} between the initial and final states are expected to have smaller magnitude due to the rapid oscillation of $\sin(\mathbf{k} \cdot \boldsymbol{\rho})$ and $\cos(\mathbf{k} \cdot \boldsymbol{\rho})$ in space. Dynamic dipolar field contribution to the correction should have comparable magnitude to the static one, if we notice that the dynamic correction is just the integral of the static one multiplied by a small number of the order of θ .

III. NEGATIVE PARITY BANDS

To obtain the n_y^- bands, we need to use $wk_y = \pm(n_y - 1/2)\pi, n_y = 1, 2, \dots$ for the expansion of wave function. For micromagnetic simulation, the y -profile of excitation field was changed to $f = \text{sinc}(k_y^c y_r/2) \sin(k_y^c y_r/2)$ to approximate an antisymmetric uniform distribution in k_y up to k_y^c . Other parameters remained the same as for the n^+ bands. Thus obtained frequency bands are shown in Figs. S4, S5, and S6. The spin-wave distribution for the n_y^- DE mode is given in Fig. S7

IV. STATIC DEMAGNETIZATION FIELD

The static dipolar, or demagnetization, field for the slab dimension considered in the main text can be analytically calculated by integrating the Green function given therein over the slab region. The explicit expression for the integration of the zz component is

$$2\pi d_0^z = w_+ \ln \frac{\sqrt{1 + w_+^2 + l_+^2} - l_+}{\sqrt{1 + w_+^2 + l_-^2} + l_-} \frac{\sqrt{w_+^2 + l_-^2} + l_-}{\sqrt{w_+^2 + l_+^2} - l_+} + l_+ \ln \frac{\sqrt{w_+^2 + l_+^2} + w_+}{\sqrt{1 + w_+^2 + l_+^2} + w_+} + l_- \ln \frac{\sqrt{w_+^2 + l_-^2} + w_+}{\sqrt{1 + w_+^2 + l_-^2} + w_+} + \tan^{-1} \frac{l_- w_+}{\sqrt{1 + w_+^2 + l_-^2}} + \tan^{-1} \frac{l_+ w_+}{\sqrt{1 + w_+^2 + l_+^2}}$$

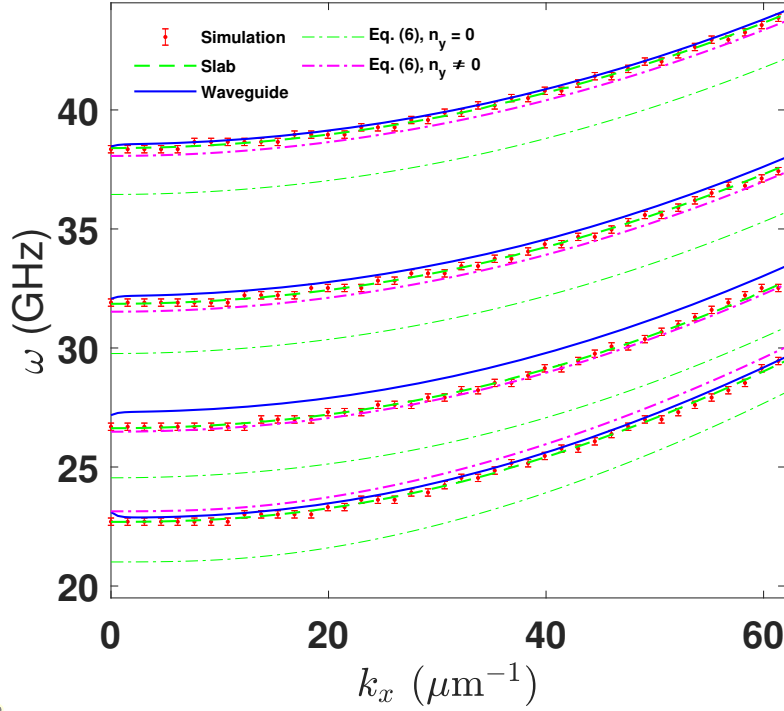


FIG. S4. n^- bands for a monolayer CrSBr waveguide in the notation of Fig. 3.

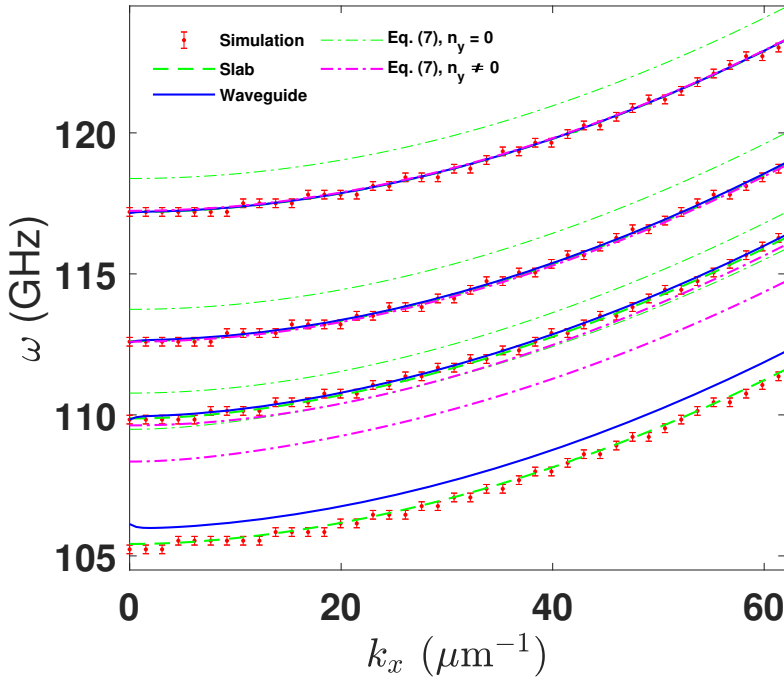


FIG. S5. n^- bands for a monolayer CrSBr waveguide in the notation of Fig. 4.

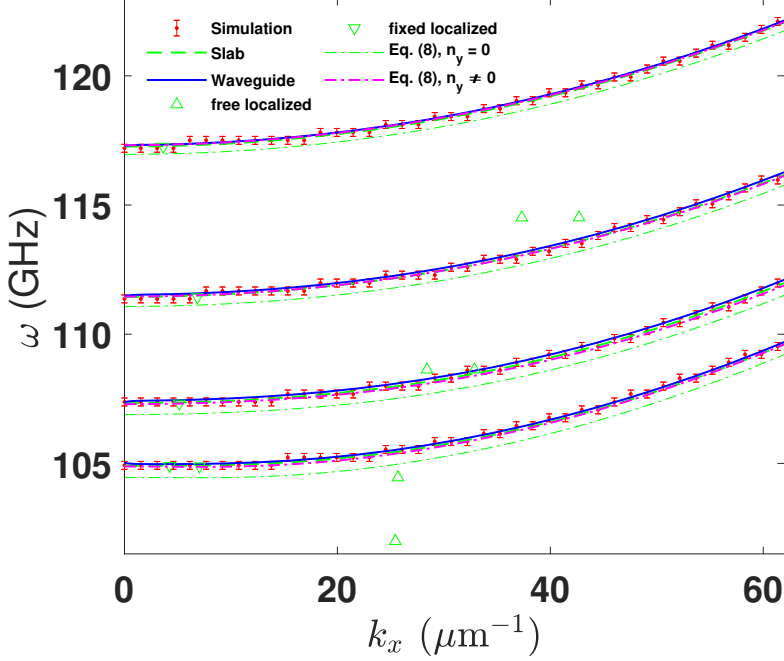


FIG. S6. n^- bands for a monolayer CrSBr waveguide in the notation of Fig. 5.

$$+(y \rightarrow -y) + l_+ \ln(1 + l_+^{-2}) + l_- \ln(1 + l_-^{-2}), \quad (S6)$$

where $l_{\pm} = (l \pm x)/2t$. For the yy component, the integration gives

$$2\pi d_0^y = w_+ \ln \frac{\sqrt{1 + w_+^2 + l_+^2} + l_+}{\sqrt{1 + w_+^2 + l_-^2} - l_-} \frac{\sqrt{w_+^2 + l_-^2} - l_-}{\sqrt{w_+^2 + l_+^2} + l_+} - \tan^{-1} \frac{2w_+}{1 - w_+^2} + \tan^{-1} \frac{l_- \sqrt{1 + w_+^2 + l_-^2} + l_-^2 + w_+^2}{w_+} + \tan^{-1} \frac{l_+ \sqrt{1 + w_+^2 + l_+^2} + l_+^2 + w_+^2}{w_+} + (y \rightarrow -y). \quad (S7)$$

$-d_0^z$ and $-d_0^y$ corresponds to the static demagnetization field acting on the magnetization when it is uniformly magnetized along \hat{z} and \hat{y} , respectively. The demagnetization field for magnetization along \hat{x} can be obtained using the constraint $d_0^x + d_0^y + d_0^z = 1$. They are symmetric under inversion along both x and y . Due to the long-range character of the dipolar field, the slope of d_0^z at the four equivalent corners $x = \pm l$ and $y = \pm w$ is infinite, the value of d_0^y depends on the path taken to approach the corners, and d_0^x has both singular features. Their distribution is plotted in Figs. S8, S9, and S10. Integration of the off-diagonal element G_{xy} gives the antisymmetric demagnetization field,

$$2\pi d_0^{xy} = \sqrt{1 + l_+^2 + w_+^2} - \sqrt{1 + l_-^2 + w_+^2} + \sqrt{l_-^2 + w_+^2} - \sqrt{l_+^2 + w_+^2} + \ln \sqrt{\frac{w_+^2 + l_+^2}{w_+^2 + l_-^2}} \frac{\sqrt{1 + w_+^2 + l_-^2} + 1}{\sqrt{1 + w_+^2 + l_+^2} + 1} - (y \rightarrow -y). \quad (S8)$$

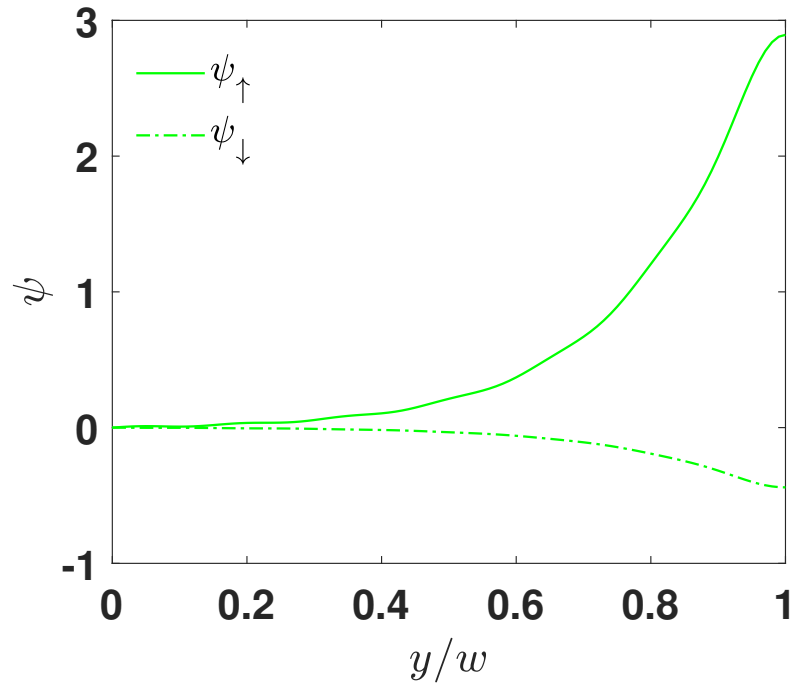


FIG. S7. Spin-wave wave function of the DE state with $k_x = 0$.

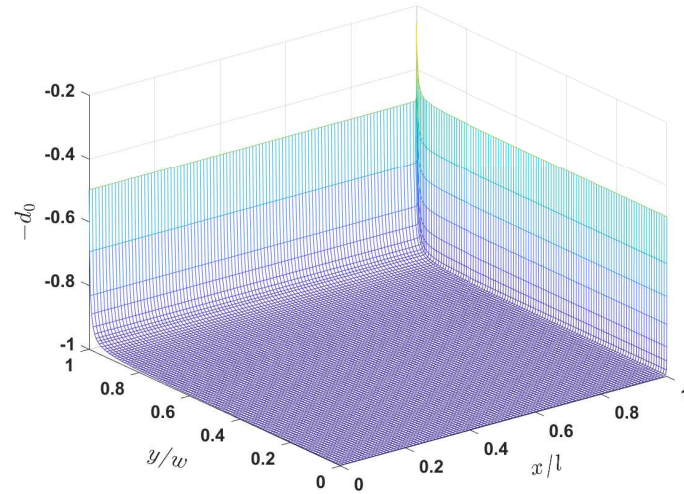


FIG. S8. Demagnetization field $-d_0^z$ for the slab dimension in the main text.

d_0^{xy} is divergent at the corners of the slab. Due to the presence of d_0^{xy} , a uniform state magnetized in-plane is unstable against magnetization curling.

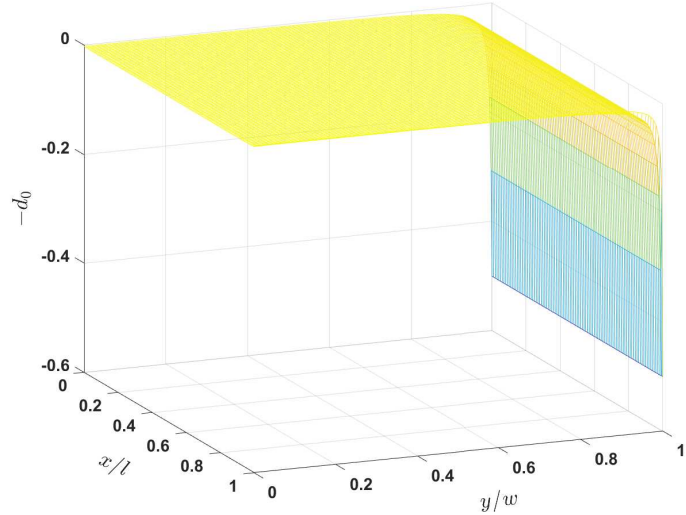


FIG. S9. Demagnetization field $-d_0^y$ for the slab dimension in the main text.

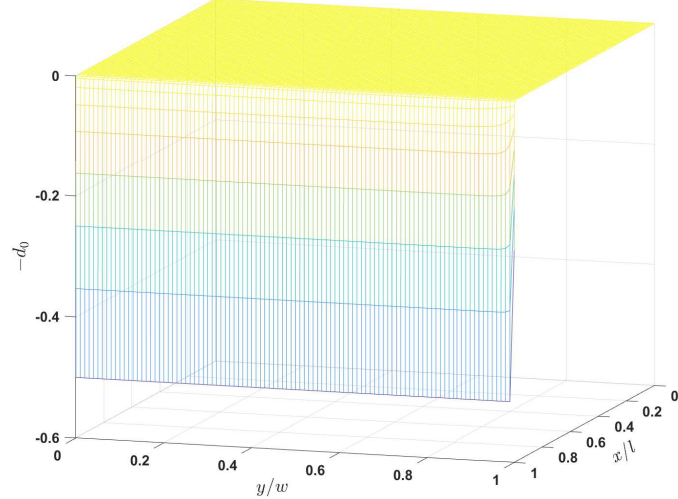


FIG. S10. Demagnetization field $-d_0^x$ for the slab dimension in the main text.

V. LOCALIZED STATES

Theoretically calculated spin-wave distribution for the lowest fixed and free localized states when $\hat{h}_a = \hat{x}$ is shown in Figs. S11 and S12.

To observe the localized states in simulation, an oscillating field with frequency f localized in one mesh cell at the boundary at $x = \pm l$ was applied, and the corresponding Fourier transform at the frequencies of the lowest localized states was obtained to extract the spin-wave amplitude. For n_y^+ states, the excitation field is uniform in y , while it is antisymmetric

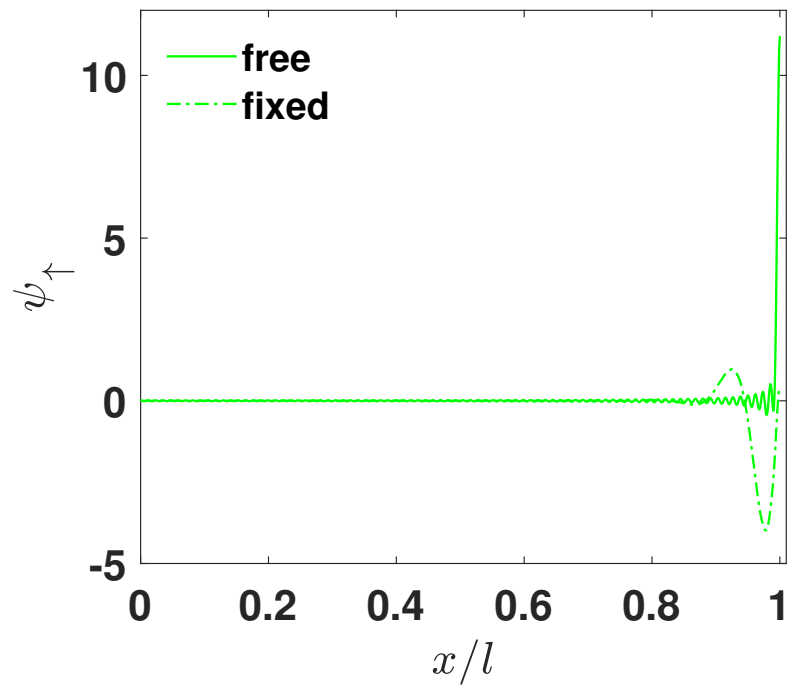


FIG. S11. Spin-wave amplitude at $y = 0$ of the lowest free and fixed n^+ states in Fig. 5.

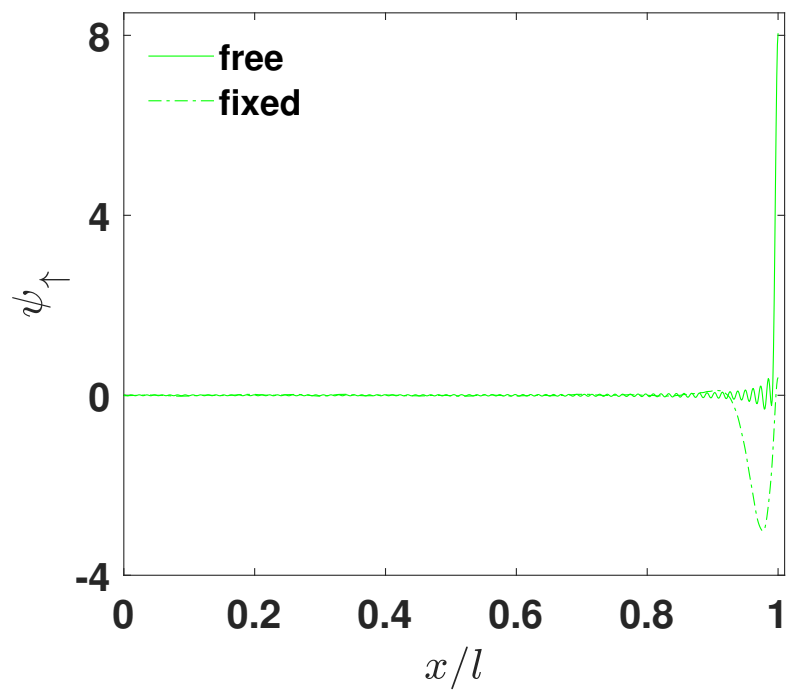


FIG. S12. Spin-wave amplitude at $y = w$ of the lowest free and fixed n^- states in Fig. S6.

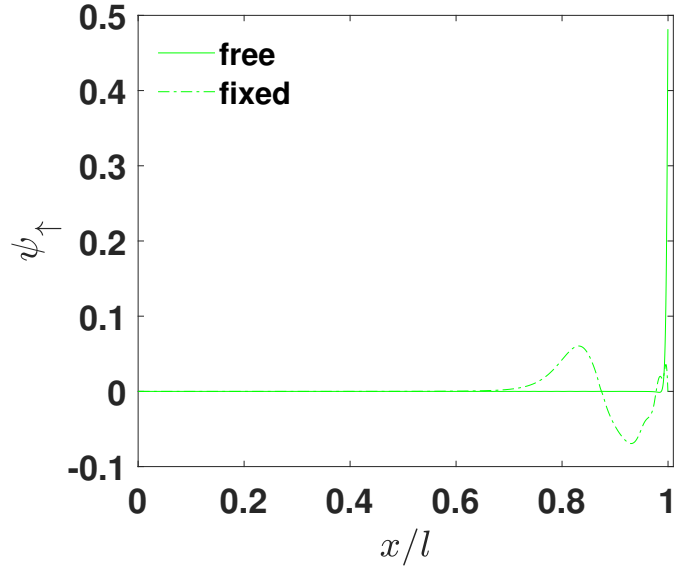


FIG. S13. P_y^+ and P_x^+ localized states from micromagnetic simulation at $y = \pm\Delta/2$. The frequency of the free (fixed) localized state is 16.0 (16.7) GHz.

in y with the sinusoidal profile $\sin \pi y_r/2$ around $y = 0$. The obtained spin-wave distribution, after factoring out a high- k_x component, is shown in Figs. S13 and S14. The states correspond to the free boundary condition agree well with the theoretical calculation, but the agreement between states with fixed boundary condition is only qualitatively, especially for the n_y^- state in Fig. S14. One probable reason is the close vicinity of the localized states' frequency to the propagating states and to each other, as shown in Fig. S6.

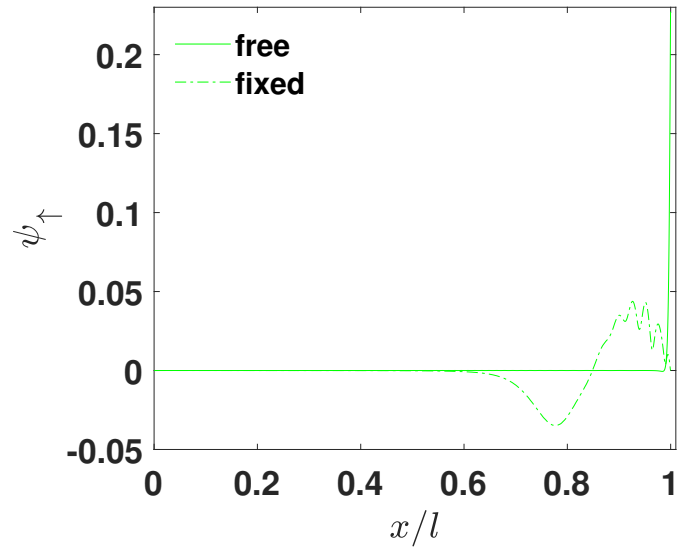


FIG. S14. P_y^- and P_x^+ localized states from micromagnetic simulation at $y = \pm(w - \Delta/2)$. The frequency of the free (fixed) localized state is 16.1 (17.1) GHz.